RSC Advances

PAPER

View Article Online
View Journal | View Issue

Cite this: *RSC Adv.*, 2024, **14**, 9529

Development of dual-channel fluorescent mesoporous SiO_2 nanosphere-coated yttrium aluminum garnet composites for sensitive detection of latent fingerprints

Ping Yang, * Tingfei Shi, Shuangquan Zhu, Kuiliang Li and Hong Zhao

Received 26th January 2024
Accepted 14th March 2024

DOI: 10.1039/d4ra00676c

rsc.li/rsc-advances

In this study, we investigated the detection of latent fingerprints (LFPs) using green light- and near-infrared (NIR) light-induced up/down-conversion dual-channel composites. Upconverted yttrium aluminium garnet (YAG) was prepared using a citric acid-assisted sol–gel method. After loading rhodamine 6G (RhD-6) into mesoporous silica nanospheres (MSNs), the MSNs-RhD-6 composites were coated with the as-synthesised YAG *via* electrostatic adsorption using the layer-by-layer method, demonstrating reversible switching between yellow and green light waves under 525 nm green light or 980 nm laser excitation. To evaluate the effectiveness of YAG-MSNs-RhD-6 powder in criminal investigations, we conducted simulations for different fingerprint scenarios. The results indicated that even after prolonged aging (up to 20 days), exposure to water, or high-temperature baking, the fingerprints remained clearly visible in the images. The detection of LFPs on various substrate surfaces exhibited high contrast, with the details of the fingerprints easily observable even after appropriate magnification. This study opens a new path for green light- and near-infrared light-induced up/down-conversion dual-channel composites for optical applications.

1 Introduction

In the fields of criminal investigation and forensic chemistry, the identification of suspects specifically relies on the discovery of traces and biological information left behind.[1–4] Certain biological characteristics such as fingerprints, DNA, voiceprints, and birthmarks are unique to each individual and serve as valuable tools for identification.[5–7] Among these characteristics, fingerprints are particularly effective in identifying a person. However, latent fingerprints (LFPs) are often invisible to the naked eye and require visualisation methods for detection.[2–4] Various methods, such as powder dusting, cyanoacrylate/iodine fumigation, spraying, and fluorescent staining, can be used to enhance LFP visibility. Powder dusting, in particular, is a convenient and efficient method.[8] Nevertheless, common powders have limitations such as toxicity, low luminescence efficiency, weak adhesion, and background interference.[9–11] ZnO:Ca, which is easy and cheap to synthesise, can emit both visible and near-infrared light and can also be used as an LFP detector,[12,13] but owing to its relatively large molecular size, it can cover some pores on the fingerprint during development, causing the fingerprint to lose detail. To address these drawbacks, Komahal *et al.* synthesised spherical core–shell SiO_2@$ZnAl_2O_4$:Eu^{3+} (5 mol%) nanophosphors (NPs) using a solvent-thermal method.[14] These NPs were utilised to develop fingerprints under UV light irradiation. Deepthi *et al.* reported the preparation of Eu(III)-doped CeO_2 for LFP detection.[15] However, single-channel-based NPs are susceptible to interference from external factors such as the light source and substrate surface texture, which can lead to inaccurate LFP detection. To overcome these limitations, the use of composites based on up/down conversion dual-channel core–shell fluorescent nanoparticles is recommended.[16–18] These composites offer nontoxicity, high luminescence efficiency, high adhesion, and the ability to produce high-contrast images, even on rough surfaces.

Rare earth element-doped fluorescent nanoparticles have been extensively studied for their potential applications in biosensors, biotags, LFP detection, anti-counterfeiting, and light-emitting devices.[19–23] Yb- and Er-doped rare-earth ion-doped yttrium aluminium garnet (YAG) crystals were chosen to obtain the advantages of good thermochemical stability, high fluorescence conversion efficiency, low vibrational energy, and ease of synthesis.[24–26]

As a traditional organic dye, the poor photochemical stability, severe photobleaching, and photodegradation phenomena significantly limit the application of rhodamine 6G (RhD-6) in fluorescent labelling.[27] Silicon dioxide has good chemical inertness and optical properties, and encapsulating fluorescent dyes within silicon dioxide cores to obtain

School of Chemical and Blasting Engineering, Anhui University of Science and Technology, Huainan, Anhui, 232001, P. R. China. E-mail: pyang8066@163.com

functionalised SiO_2 fluorophores solves the limitations of fluorescent dyes.[28–31] The Stöber process allows precise control over the morphology and size of silica particles, enabling control over the fluorophore by manipulating the particle size of silica.[30,32] Moreover, the use of silicon dioxide, which is cheaper than most fluorescent materials, makes the composite SiO_2 fluorescent material more affordable than pure fluorescent material per unit mass. To enhance the accuracy and applicability of LFP detection, up-converting and down-converting materials are combined through electrostatic adsorption to create up/down-converting dual-channel composites.[33–35] These composites are excited by multiple light sources, such as green and near-infrared (NIR) light, thereby improving the overall performance of LFP detection.

In this study, RhD-6 was embedded in mesoporous silica nanospheres (MSNs) to enhance their photochemical stability and adhesion to the LFP of the composites. Rare earth element-doped YAG was synthesised using the citric-acid-assisted sol–gel method. A layer-by-layer method was employed to coat YAG with MSNs-RhD-6,[36] preparing 525 nm green light and 980 nm NIR light-induced up/down conversion dual-channel YAG-MSNs-RhD-6 composites. The optical properties of the resulting materials were thoroughly investigated and characterised. Detecting LFP using multiple light sources avoids the influence of a single light source on the background of the substrate and improves the accuracy of fingerprint detection. Practical applications were demonstrated by conducting LFP detection even after being subjected to high temperatures, water, and aging rinsing. The results indicated that the fingerprint details were clearly recognisable.

2 Experimental

2.1 Materials and instruments

Yttrium oxide (Y_2O_3), ytterbium oxide (Yb_2O_3), erbium oxide (Er_2O_3), aluminum nitrate nonahydrate ($Al(NO_3)_3 \cdot 9(H_2O)$), 3-aminopropyltriethoxysilane (APTES), poly(sodium-4-styrenesulfonate) (PSS) and polyethyleneimine (PEI) were purchased from Aladdin Reagent Co. in Shanghai, China. Cetyltrimethylammonium bromide (CTAB), tetraethyl orthosilicate (TEOS), triethanolamine (TEA), sodium hydroxide, sodium fluoride, anhydrous ethanol, concentrated nitric acid and concentrated hydrochloric acid were supplied by Sinopharm Chemical Reagent Co. (Shanghai, China). Nanoscale calcium carbonate was provided by Shanghai McLean Biochemical Technology Co. All chemicals were of analytical grade and used without further purification. The commercial fluorescent powder used for the comparison experiments was purchased from Beijing Fingal Huaan Technology Co. The 525 nm green light source was emitted by a homemade lamp with 5 W power. A 980 nm laser light source was a homemade laser emission, with a power of 5 W, through the homogeniser to expand the light spot. Photoluminescence (PL) spectra were obtained using a Cary Eclipse FL1011M003 (Varian) fluorescence spectrometer. The morphology of YAG-MSNs-RhD-6 was characterised using transmission electron microscopy (TEM, JEOL 2010F). X-ray diffraction (XRD, Cu Kα = 1.5418 Å radiation) was performed using a PANalytical X-Pert instrument.

2.2 Preparation of amino MSNs-RhD-6

MSNs-RhD-6 was prepared using a modified $CaCO_3$-assisted sol–gel method. RhD-6 (8 mg), $CaCO_3$ (10 mg), CTAB (0.5 g), and TEA (80 mg) were dissolved in 20 mL of deionised water, stirred at 90 °C for 6 h, and then 3 mL of TEOS was added dropwise, and stirring was continued for 3 h. The precipitate was then centrifuged and washed several times with ethanol. It was then dried under vacuum for 12 h to obtain the $CaCO_3$@SiO_2-RhD-6 nanospheres. Thirty milligrams of $CaCO_3$@SiO_2-RhD-6 powder was taken in a round bottom flask, and 40 mL of ethanol was added to it. Hydrochloric acid was used to adjust the pH to 4, and the mixture was heated to 76 °C in an oil bath with stirring and refluxing for 6 h. The resulting reaction mixture was washed with ethanol thrice and then dried in a vacuum drying oven at 60 °C for 12 h to obtain MSNs-RhD-6 powder. Thirty milligrams of MSNs-RhD-6 powder was placed in a round-bottomed flask containing 40 mL of ethanol, 1 mL of APTES was added, and heated to 76 °C in an oil bath with stirring and refluxing for 6 h. Then, the excess APTES was washed with ethanol and finally dried in vacuum at 60 °C for 12 h to obtain the amino carbonated MSNs-RhD-6.[37]

2.3 Preparation of YAG:Yb/4%Er

Preparation of rare earth nitrates for YAG:Yb/Er synthesis. Y_2O_3 (0.2574 g), Yb_2O_3 (0.1182 g), and Er_2O_3 (0.0230 g) were mixed with enough amount of nitric acid, and the excess nitric acid solution and water were evaporated to obtain the rare-earth nitrates, which were then collected and set aside. Rare earth ion-doped yttrium aluminium garnet particles (YAG:Yb/Er) were prepared by the citric acid-assisted sol–gel method, followed by heat treatment. The above-prepared rare earth nitrate was dissolved with 1.8757 g of $Al(NO_3)_3 \cdot 9H_2O$ and 3.0739 g of citric acid in 40 mL of deionised water (the molar ratio of metal ions to citric acid was 1 : 2), covered with a plastic wrap, and stirred continuously for 30 min to form a homogeneous and transparent liquid at 80 °C. Subsequently, the plastic wrap was removed, and the solvent was allowed to evaporate. A yellowish wet gel formed within 2 h, allowing the solvent to evaporate. The wet gel was dried at 200 °C for 2 h to obtain a porous solid matrix. To obtain YAG:Yb/4%Er phosphors, the dried gel samples were first calcined at 1500 °C (rate: 5 °C min^{-1}) for 5 h and then annealed at 1500 °C (rate: 10 °C min^{-1}) for 5 h. Lanthanide oxides (Y_2O_3, Yb_2O_3, and Er_2O_3) were prepared by varying the amount of lanthanide oxides (Y_2O_3, Yb_2O_3, and Er_2O_3) added, while the rest remained unchanged using the same method for the preparation of different Er(III) YAG with different Er(III) doping concentrations (2%, 3%, 3.5%, and 5%).

2.4 Preparation of YAG-MSNs-RhD-6

According to our previously reported method, polyelectrolytes (PSS/PEI/PSS) are adsorbed alternately on the YAG layer-by-layer,[36] resulting in a negatively charged YAG:Yb/4%Er (8 mg) and 20 mg of amino MSNs-RhD-6 [$m(YAG^-) : m(MSNs\text{-}RhD\text{-}6) =$

2 : 5] were added to 10 mL of deionised water and incubated for 4 h in the dark after thorough mixing. The precipitate was collected by centrifugation, washed three times with a mixture of deionised water and ethanol (v : v = 1 : 1), and finally dried under vacuum for 24 h to obtain the YAG-MSNs-RhD-6 powder.

2.5 Dual-channel YAG-MSNs-RhD-6 composites to detect potential handprints

A single donor donated all the fingerprints used in this study. Before pressing the fingerprints onto the substrates, hands were washed thoroughly with soap. The fingers were then placed in contact with the forehead before gently pressing them onto the surfaces of the different substrates. For the detection of latent fingerprints using the YAG-MSNs-RhD-6 powder, the powder was first processed by grinding and filtering out large particles using a 150-mesh sieve. It was then dried and lightly brushed onto the imprinted LFP using a feather brush to develop the image. The excess powder was removed by blowing it off with a wash ball. The fingerprints were then photographed using a Sony α6000 camera under 525 nm green light and 980 nm laser excitation. The fingerprint details were subsequently analysed using ImageJ, a free software program developed by the National Institute of Health.

3 Results and discussion

3.1 Characterisation of dual-channel YAG-MSNs-RhD-6

As shown in Scheme 1, YAG doped with rare earth elements was synthesised using the citric-acid-assisted sol–gel method. RhD-6 was coated onto MSN to obtain the MSNs-RhD-6 nanosphere. After loading the polymers PEI and PSS onto YAG by the layer-by-layer method, a dual-channel YAG-MSNs-RhD-6 composite was prepared through electrostatic adsorption with the advantages of excellent fluorescence performance, large specific surface area, and high adhesion. The composites were used to detect LFP in different substrates and environments.

To investigate the composition and structure of the composites, the YAG:Yb/4%Er NPs were subjected to XRD. The

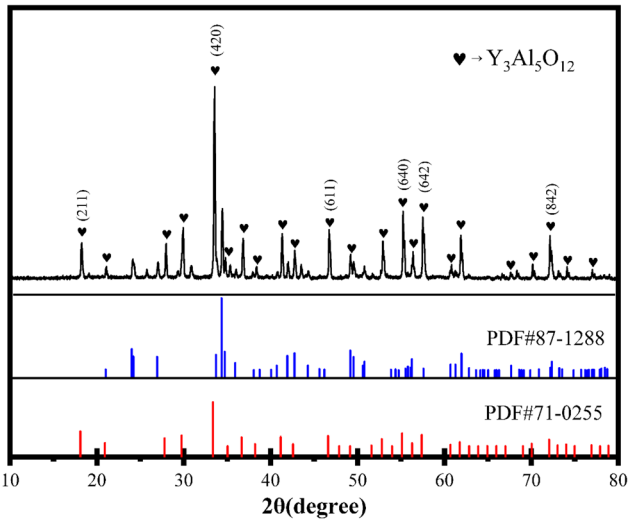

Fig. 1 X-ray diffraction pattern of YAG-MSNs-RhD-6.

experimental results and YAG crystal standard card (71-0255) are shown in Fig. 1. The YAG:Yb/4%Er NPs have obvious characteristic diffraction peaks, and the diffraction peaks at 2θ = 18.083°, 33.349°, 46.593°, 55.115°, 57.384°, and 72.039° correspond to the (211), (420), (611), (640), (642), and (842) crystal planes, respectively, of YAG. Because the generation of YAG at high temperatures is a multiphase reaction, the samples contain a small number of diffraction peaks of $YA1O_3$,[38] corresponding to the standard card (87-1288).

The morphology and structure of the YAG and YAG-MSNs-RhD-6 composites were studied using SEM and TEM. From Fig. 2a, it can be seen that the YAGs are all irregular polygonal granular structures, the grains do not grow abnormally, and the grain size distribution is uniform, indicating that they are still yttrium–aluminium garnet phases, which agree with the XRD results. Fig. 2b shows the SiO_2 nanospheres coated onto the YAG surface. Fig. 2c shows TEM images of pure YAG with a size of 100 nm. The mesoporous structure of the SiO_2 can be observed in Fig. 2d. As shown in Fig. 2e, mesoporous

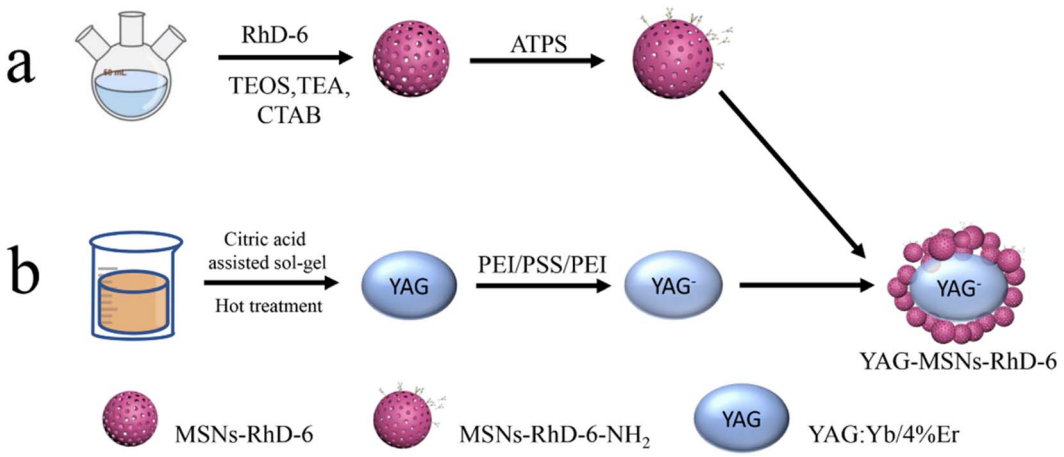

Scheme 1 Synthesis of YAG-MSNs-RhD-6 composites for LFP detection by powder dusting method.

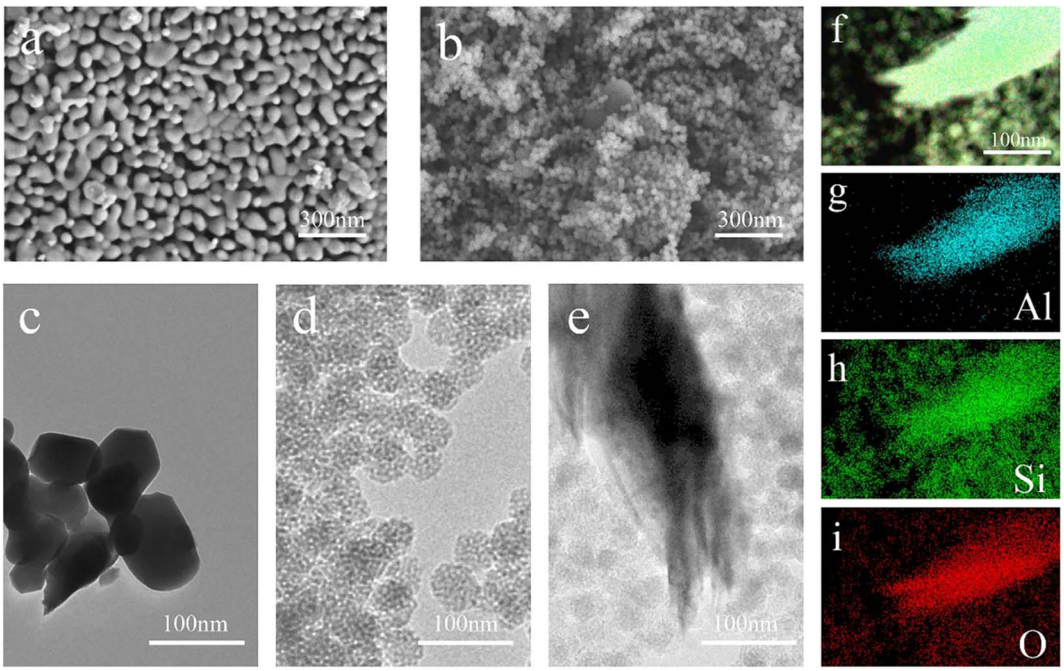

Fig. 2 SEM images of YAG (a) and YAG-MSNs-RhD-6 (b); TEM images of YAG (c), MSNs-RhD-6 (d), and YAG-MSNs-RhD-6 (e); EDS energy spectra of YAG-MSNs-RhD-6 composites (f–i).

nanospheres were loaded onto the surface of the metal-based compound. The mapping results in Fig. 2f–i show that Al is mainly distributed in YAG, whereas Si and O are uniformly distributed in SiO_2.

3.2 Fluorescence properties of dual-channel YAG-MSNs-RhD-6 composites

Fig. 3a shows the fluorescence spectrum of MSNs-RhD-6, whose optimal excitation wavelength (λ_{ex}, max) is 528 nm; therefore, 525 nm green light was chosen as the down-conversion light source. The maximum emission wavelength (λ_{em}, max) was 560 nm, which corresponds to the yellow-green fluorescence. The effect of the Er(III) content on the upconversion fluorescence intensity was optimised. As shown in Fig. 3b, the emission intensity increased when the Er(III) doping concentration was increased from 2% to 4% under 980 nm laser excitation. When the Eu(III) doping concentration was further increased to 5%, the emission intensity decreased significantly owing to the concentration burst effect. Up-conversion fluorescence analysis revealed that the optimum concentration of Er(III) was 4%. Therefore, 4% Er was used as the upconversion material for the YAG-MSNs-RhD-6. Moreover, the up-conversion emission spectra of YAG:Yb/4%Er were mainly in the range of 517–566 nm, with a maximum wavelength (λ_{em}, max) of 545 nm, which corresponds to the green colour. Furthermore, the effect of the mass ratio of the YAG and MSNs-RhD-6 on the fluorescence intensity was investigated. Fig. 3c shows that the fluorescence intensity increased with increasing mass ratio of YAG:Ce and MSN-RhD-6 in the composites under irradiation with 525 nm green light. As shown in Fig. 3d, the fluorescence intensity decreased with increasing mass ratio of YAG:MSN-RhD-6 in the composites under the irradiation of 980 nm. Thus, a mass ratio of m(YAG) : m(MSNs-RhD-6) of 5 : 2 was used for balanced fluorescence performance under 525 nm green light and 980 nm NIR. Therefore, a ratio of m(YAG) to m(MSNs-RhD-6) in the YAG-MSNs-RhD-6 composite at 5 : 2 was used for LFP development.

3.3 Developing LFPs using dual-channel YAG-MSNs-RhD-6 composites

The application for the detection of LFP was evaluated using dual-channel YAG-MSN-RhD-6 composites. Various common items, such as courier bags, marbles, iron sheets, glass, crucibles, frosted plastic boxes, and blue plastic boxes, were chosen as substrates for the LFP (Fig. 4). The properties of the substrate surface, including colour, pattern, and flatness, were found to affect the visibility of the LFP development. The experimental results demonstrated that LFPs on courier bags, marble, iron sheets, glass, and frosted plastic boxes could be effectively visualised under 525 nm green light (Fig. 4a–d and f) or 980 nm laser light (Fig. 4a′–d′ and f′). However, the LFPs on the crucibles showed poorer contrast owing to the background effect of the crucible itself, although the LFP contours were still distinguishable (Fig. 4e and e′). As shown in Fig. 4f and f′, it is difficult to distinguish the fingerprints under 525 nm green light owing to the influence of the blue plastic box background, but the outline of the fingerprints can be clearly shown under the 980 nm laser. The results show that the dual-channel YAG-MSNs-RhD-6 composite can eliminate the influence of the substrate background and obtain high-quality LFP fluorescence images, even on rough surfaces such as marble (Fig. 4b and b′),

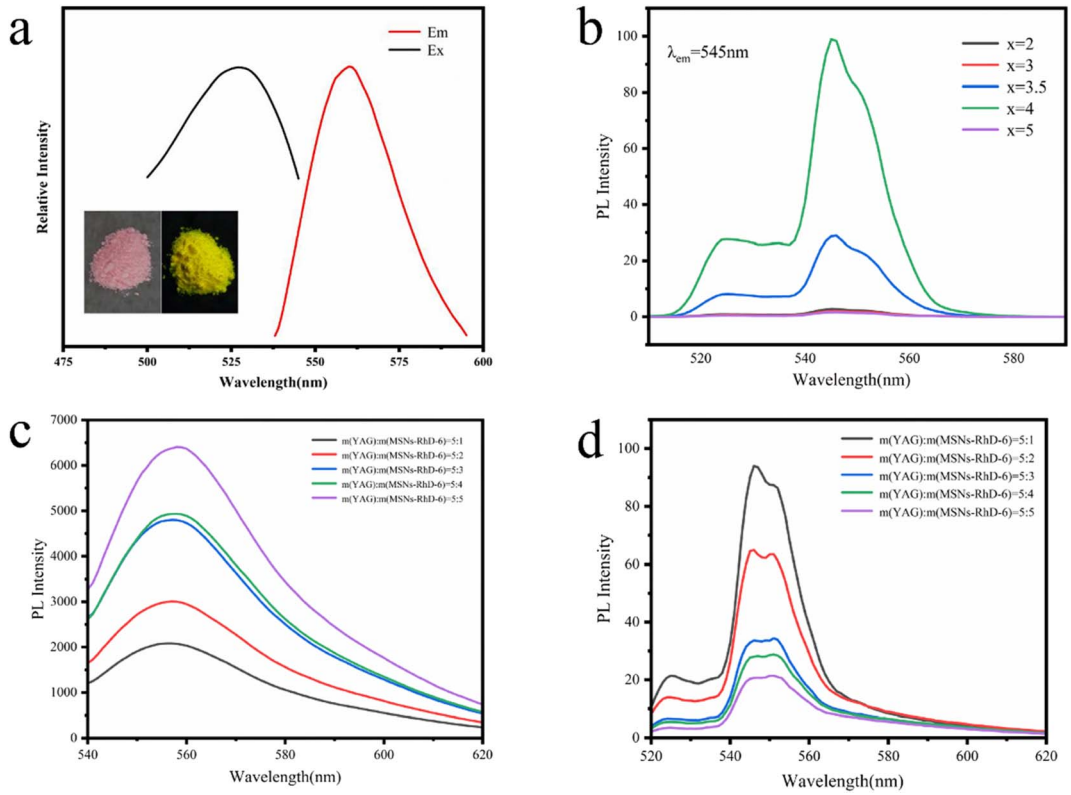

Fig. 3 (a) Excitation (Ex) and emission (Em) spectra of MSNs-RhD-6 (λ_{ex} = 528 nm, λ_{em} = 560 nm); (inset) photographs of MSNs-RhD-6 powder under natural light (left) and 365 nm UV light (right). (b) YAG emission spectra with different Er(III) doping concentrations (2%, 3%, 3.5%, 4% and 5%) under 980 nm laser excitation; emission (Em) spectra of YAG:Yb/4%Er (λ_{em} = 545 nm); (c and d) emission spectra of YAG-MSNs-RhD-6 composites synthesized by YAG and MSNs-RhD-6 at different mass ratios under 525 nm green light and 980 nm laser excitation, respectively.

crucibles (Fig. 4e and e′), and frosted plastic boxes (Fig. 4f and f′).

Fingerprint recognition relies on the analysis of detailed fingerprint features. These features are divided into three tiers, with the second tier being the most commonly used and valuable for identification purposes. YAG-MSNs-RhD-6 powder, known for its effective adsorption on fingerprints rich in water and fatty acids, can immobilise the ridge and groove structures of the fingerprint. This immobilisation technique enables the visualisation of important structures such as secondary bifurcations, terminations, islands, and breakpoints, which are crucial for forensic identification. This study demonstrates that

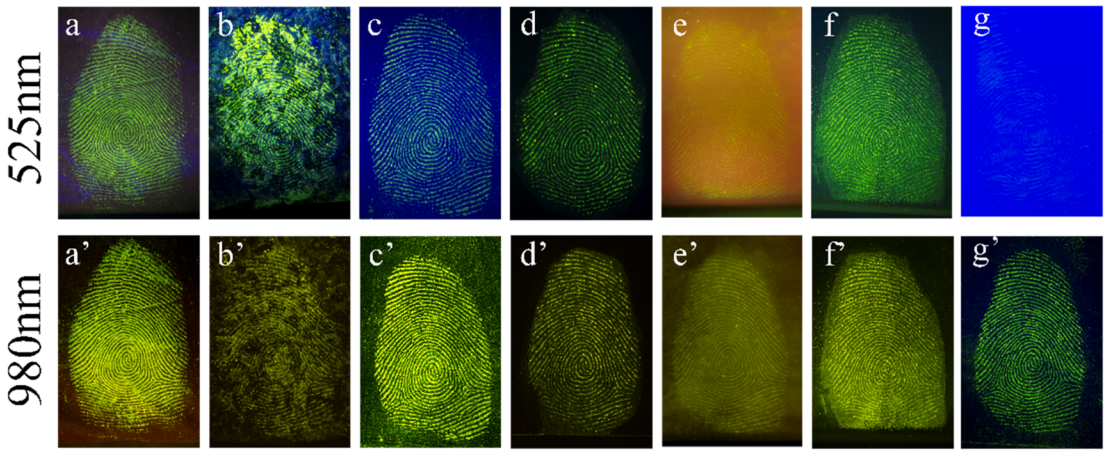

Fig. 4 Latent fingerprints formed on different substrates with 525 nm green light (top row) and 980 nm laser (bottom row). Substrates: courier bags (a and a′), marble (b and b′), iron sheets (c and c′), glass (d and d′), crucibles (e and e′), frosted plastic boxes (f and f′) and blue plastic boxes (g and g′).

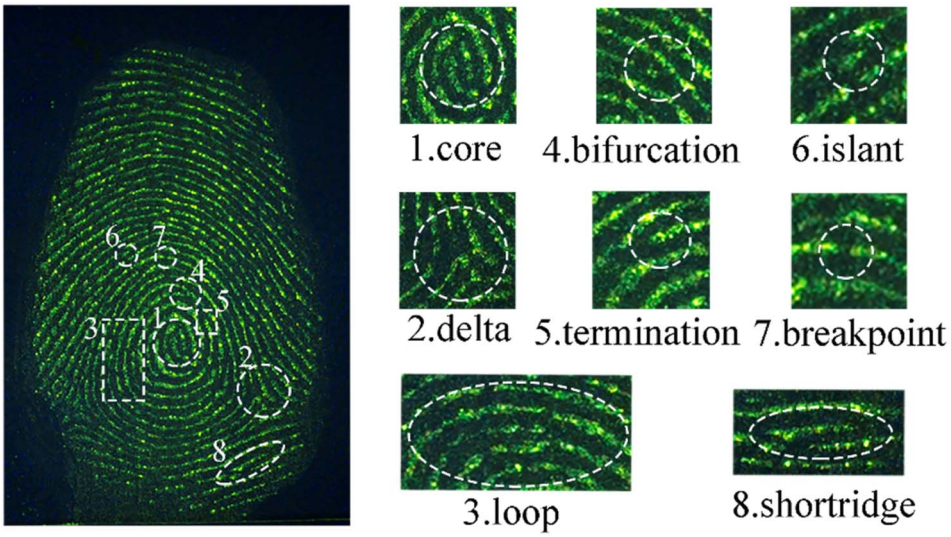

Fig. 5 Some details of latent fingerprints on glass prepared with YAG-MSNs-RhD-6 powder under 525 nm green light.

detailed fingerprint images captured under both 525 nm green light and 980 nm NIR exhibit clear localised features. In Fig. 5 and 6, we observe distinct details such as nuclei, triangles, and loops, whereas macroscopic features such as ridge and furrow patterns, including bifurcations, terminations, islands, breakpoints, and short ridges, are enhanced when appropriately enlarged.

To validate the utility of YAG-MSNs-RhD-6-based LFP detection methods in forensic science, we conducted experiments to simulate the conditions encountered during crime investigations. We subjected the LFP to high temperatures, washing, and aging. High temperatures increase the water loss from fingerprints, making LFP development more challenging. In Fig. 7a and b, the right half of the fingerprint image was developed after sizzling at a high temperature of 60 °C for 20 min, and no significant difference was observed compared to the left half of the normal LFP development. Additionally, the periodic changes in the luminescence intensity (grey-scale values) between the ridges and furrows showed more regular variations (Fig. 7c). After rinsing with water, the lipids in the fingerprints were severely lost, as shown in Fig. 7d–f. However, the outlines of the LFPs were still clearly discernible under excitation with 525 nm green light after rinsing for 10 and 20 min. The LFPs on glass were aged for 1, 5, 10, 15, and 20 days. Subsequently, the YAG-MSN-RhD-6 powder was gently applied to aged LFPs using a feather brush for development. As shown in Fig. 8, the

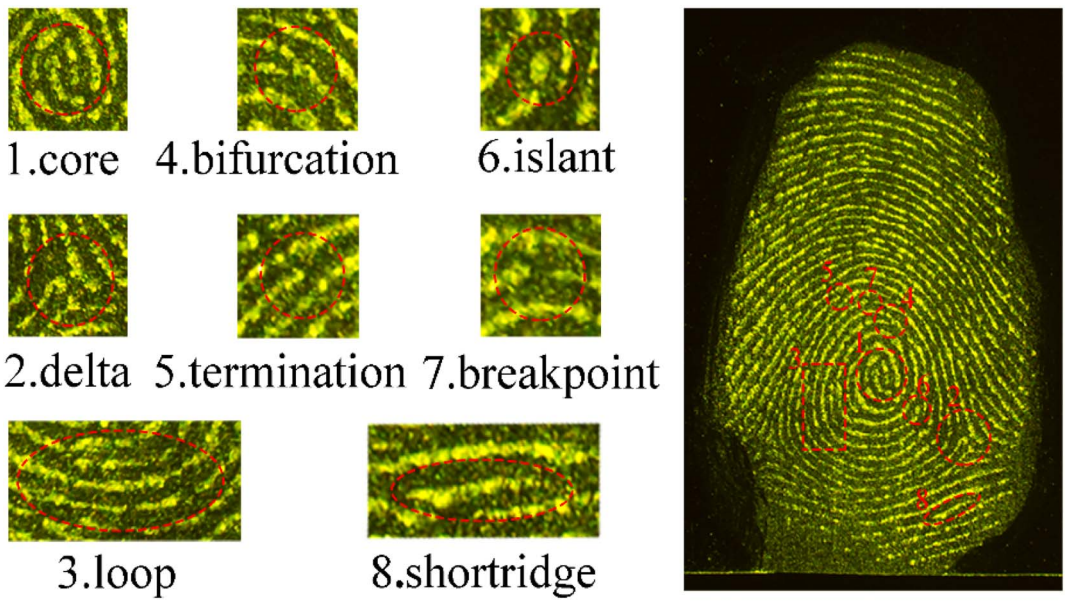

Fig. 6 Some details of latent fingerprints on glass prepared with YAG-MSNs-RhD-6 powder at 980 nm laser.

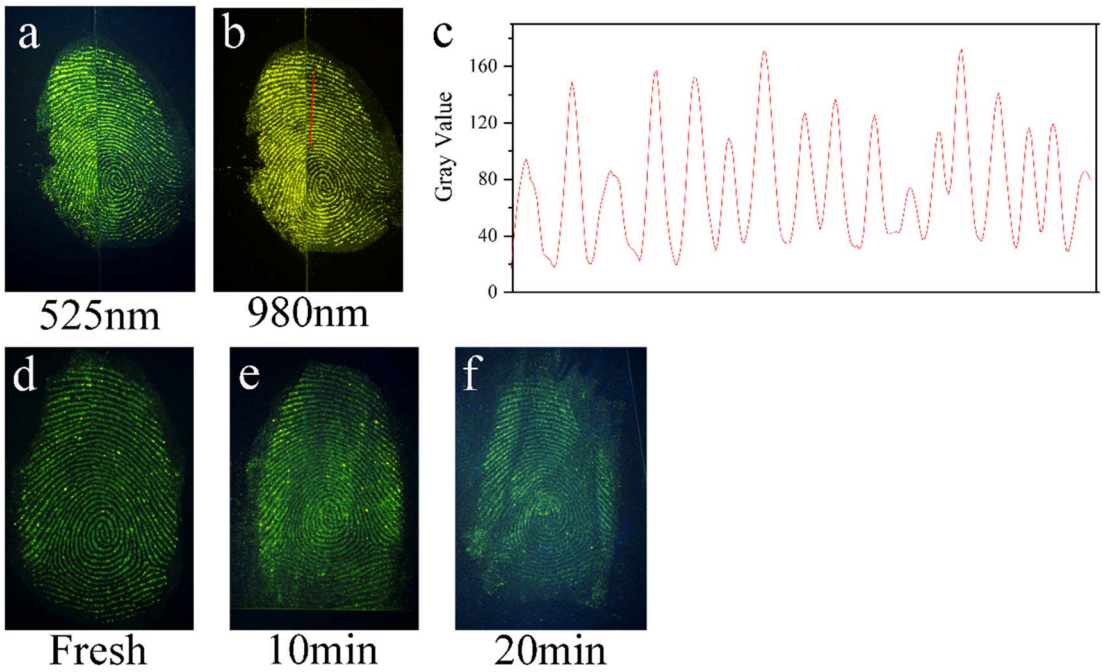

Fig. 7 The image of the latent fingerprint development with the irradiation of 525 nm green light (a) under normal condition (left) and baking at 60 °C for 20 min (right); the latent fingerprint development with the irradiation of 980 nm laser (b) under normal condition (left) and baking at 60 °C for 20 min (right); (c) the periodic change of the luminescence intensity between the ridges and grooves along the red line in (b) (grayscale value); the fluorescence images of fresh (d) with different rinsing times (e and f) latent fingerprints under 525 nm green light.

substances on the fingerprints gradually evaporated and disappeared as the aging time increased, leading to a gradual decrease in the detection sensitivity. However, even after 20 days of aging, the LFPs exhibited a clear fingerprint texture. Different interference treatments on LFP increased the complexity of LFP development, demonstrating the good sensitivity, stability, and adsorption properties of the YAG-MSNs-RhD-6 composites.

To further evaluate the potential application of the as-synthesized YAG-MSNs-RhD-6 composites for fingerprint detection, a direct comparison was conducted with a mature product currently available in the market. This comparison aimed to assess the performance of both materials in detecting

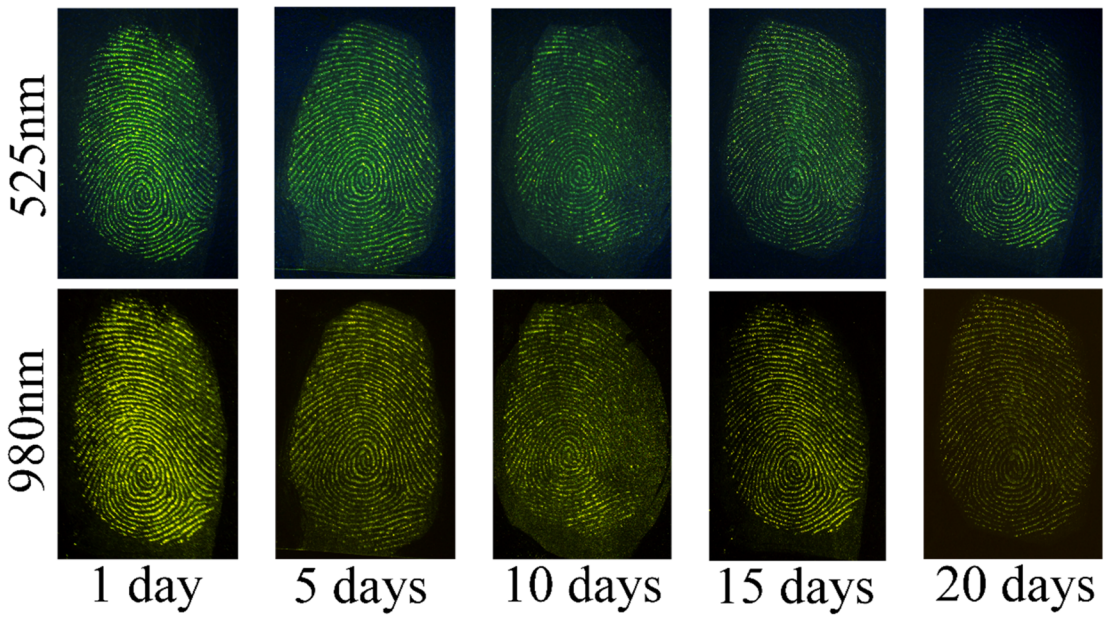

Fig. 8 The same fingerprints of YAG-MSNs-RhD-6 composites were prepared on glass under 525 nm green light (top row) and 980 nm NIR (bottom row) excitation with aging times of 1, 5, 10, 15 and 20 days, respectively.

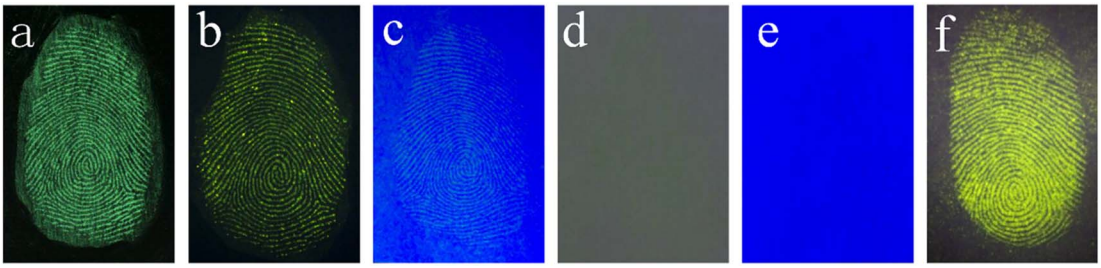

Fig. 9 The image of the latent fingerprint on glass developed with the mature product in the market (a) and the as-synthesized YAG-MSNs-RhD-6 composites (b) under the irradiation of 525 nm green light; on paper developed with the mature product in the market ((c) irradiation of 525 nm; (d) irradiation of 980 nm laser) and the as-synthesized YAG-MSNs-RhD-6 composites ((e) irradiation of 525 nm green light; (f) irradiation of 980 nm laser).

latent fingerprints on glass and paper under identical conditions. Fig. 9a demonstrates the excellent developing effect achieved by the mature product on a fingerprint left on glass when irradiated with 525 nm green light. The clear and distinct image obtained indicates that the market product is highly effective in enhancing fingerprints on glass surfaces using visible light. The as-synthesized YAG-MSNs-RhD-6 composites also showed satisfactory results for fingerprint development when irradiated with 525 nm light (Fig. 9b) on glass. However, when the fingerprint on paper was developed with the mature product in the market, it showed a poor development result under the irradiation of 525 nm green light (Fig. 9c) and 980 nm laser (Fig. 9d). Though the as-synthesized YAG-MSNs-RhD-6 composites show the same poor development result as the fingerprint on paper under the irradiation of 525 nm green light, the obvious images can be observed when irradiation the fingerprint with a 980 nm laser. Thus, the YAG-MSNs-RhD-6 composites exhibit dual channel properties, allowing them to be used for fingerprint development under different wavelengths of light. This provides flexibility and versatility in their application, making them suitable for various forensic and identification tasks.

4 Conclusion

In this study, we successfully synthesised up/down-converting dual-channel YAG-MSNs-RhD-6 composites that could be excited under 525 nm green light and 980 nm NIR light. These composites serve as novel fluorescent labelling materials for latent fingerprints on a wide range of substrates, including courier bags, marble, iron sheets, glass, crucibles, frosted plastic boxes and blue plastic boxes. We specifically investigated the development of latent fingerprints on challenging surfaces such as marble and rough plastic sheets, which have rough surfaces that make powder adhesion difficult, and background fluorescence, which affects the development of LFPs. The results showed that even after undergoing high-temperature treatment, washing, and aging, the fingerprint details were still clearly recognisable. The prepared composites exhibited high sensitivity, contrast, stability (even at high temperatures), strong adhesion, and resistance to background interference. This study presents a new avenue for the development of LFP.

Conflicts of interest

There are no conflicts to declare.

References

1 Y. Suzuki and K. Yokoyama, *Biosensors*, 2015, **5**, 337–363.
2 D. Chávez, C. R. Garcia, J. Oliva and L. A. Diaz-Torres, *Ceram. Int.*, 2021, **47**, 10–41.
3 A. a. A. Ansari, K. M. M. Aldajani, A. N. N. Alhazaa and H. a. A. Albrithen, *Coord. Chem. Rev.*, 2022, **462**, 214523.
4 V. Sharma, S. Choudhary, P. Mankotia, A. Kumari, K. Sharma, R. Sehgal and V. Kumar, *TrAC, Trends Anal. Chem.*, 2021, **143**, 116378.
5 C. Beauvineau, C. Guetta, M. P. Teulade-Fichou and F. Mahuteau-Betzer, *Org. Biomol. Chem.*, 2017, **15**, 7117–7121.
6 C. Sun, Y. Yang, C. Wen, K. Xie and F. Wen, *Sensors*, 2018, **18**, 2399.
7 F. J. Rentas and P. A. Clark, *Mil. Med.*, 1999, **164**, 785–787.
8 G. S. Sodhi and J. Kaur, *Forensic Sci. Int.*, 2001, **120**, 172–176.
9 Z. J. Qiu, B. Hao, X. G. Gu, Z. Y. Wang, N. Xie, J. W. Y. Lam, H. X. Hao and B. Z. Tang, *Sci. China: Chem.*, 2018, **61**, 966–970.
10 E. R. Menzel and K. E. Fox, *J. Forensic Sci.*, 1980, **25**, 150–153.
11 Z. Lv, Z. W. Man, Z. Z. Xu, S. Li, Q. Liao and H. B. Fu, *J. Mater. Chem. C*, 2021, **9**, 7345–7350.
12 D. Y. Medina-Velazquez, L. Garcés, B. Garces-Martinez, H. Perez-Caudillo, C. R. Garcia and J. Oliva, *Mater. Lett.*, 2023, **350**, 134975.
13 L. Garcés, C. R. Garcia, J. OlivaD and Y. Medina-Velazquez, *Opt. Mater.*, 2023, **143**, 114302.
14 P. Yang, Z. Quan, C. Li, J. Yang, H. Wang, X. Liu and J. Lin, *J. Solid State Chem.*, 2008, **181**, 1943–1949.
15 N. H. Deepthi, G. P. Darshan, R. B. Basavaraj, B. D. Prasad and H. Nagabhushana, *Sens. Actuators, B*, 2018, **255**, 3127–3147.
16 Z. Q. Xu, X. T. Huang, X. Han, D. Wu, B. B. Zhang, Y. Tan, M. J. Cao, S. H. Liu, J. Yin and J. Y. Yoon, *Chem*, 2018, **4**, 1609–1628.
17 M. G. Ren, B. B. Deng, J. Y. Wang, Z. R. Liu and W. Y. Lin, *J. Mater. Chem. B*, 2015, **3**, 6746–6752.

18 S. J. Li, P. P. Wang, M. T. Ye, K. Yang, D. Cheng, Z. Q. Mao, L. W. He and Z. H. Liu, *Anal. Chem.*, 2023, **95**, 5133–5141.
19 Y. Y. Lee, B. Sriram, S. F. Wang, S. Kogularasu and G. P. Chang-Chien, *Microchem. J.*, 2023, **193**, 109140.
20 A. Tsukamoto and T. Isobe, *J. Mater. Sci.*, 2009, **44**, 1344–1350.
21 V. D. Tan, N. B. Tong, N. T. V. Quynh, C. T. M. Dung, T. D. Chinh, L. V. T. Son, T. T. K. Hanh, P. B. Thang, L. T. T. Giang and T. T. T. Van, *Ceram. Int.*, 2023, **49**, 39993–40000.
22 G. Gao, D. Busko, R. Joseph, I. A. Howard, A. Turshatov and B. S. Richards, *ACS Appl. Mater. Interfaces*, 2018, **10**, 39851–39859.
23 T. Ogi, H. Iwasaki, A. B. D. Nandiyanto, F. Iskandar, W. N. Wang and K. Okuyama, *J. Mater. Chem. C*, 2014, **2**, 4297–4303.
24 J. A. Chen, X. G. Huang, L. X. Wang and Q. T. Zhang, *J. Rare Earths*, 2011, **29**, 44–47.
25 Q. Yao, P. Hu, P. Sun, M. Liu, R. Dong, K. F. Chao, Y. F. Liu, J. Jiang and H. C. Jiang, *Adv. Mater.*, 2020, **32**, 1907888.
26 J. Ueda, P. Dorenbos, A. J. J. Bos, A. Meijerink and S. Tanabe, *J. Phys. Chem. C*, 2015, **119**, 25003–25008.
27 S. Dumbare, A. Doshi and S. Ravindran, *Pol. J. Environ. Stud.*, 2021, **30**, 3445–3455.
28 Y. R. Hu, J. Chen, Z. X. Zhang, N. C. Zhang and D. H. Li, *Integr. Ferroelectr.*, 2016, **169**, 140–145.
29 M. Lal, L. Levy, K. S. Kim, G. S. He, X. Wang, Y. H. Min, S. Pakatchi and P. N. Prasad, *Chem. Mater.*, 2000, **12**, 2632–2639.
30 S. Chatterjee, X.-S. Li, F. Liang and Y.-W. Yang, *Small*, 2019, **15**, 1943–1949.
31 I. Pritula, O. Bezkrovnaya, A. Lopin, M. Kolybaeva, Y. Gurkalenko, V. Puzikov, V. Maslov and A. Plaksiy, *J. Sol-Gel Sci. Technol.*, 2012, **63**, 389–394.
32 A. Bilgic and A. Cimen, *J. Fluoresc.*, 2020, **30**, 867–881.
33 Q. Fei, K. Shen, H. Ke, E. Wang, G. Fan, F. Wang and J. Ren, *Bioorg. Med. Chem. Lett.*, 2023, **97**, 129563.
34 W.-J. Shi, C.-F. Li, Y. Huang, H.-Y. Tan, Y.-F. Wei, F. Liu, L.-X. Feng, L. Zheng, G.-S. Chen and J.-W. Yan, *Dyes Pigm.*, 2019, **171**, 107782.
35 H. Shao, F. Li, D. Li, Q. Ma, W. Yu, G. Liu and X. Dong, *ACS Appl. Nano Mater.*, 2022, **5**, 3333–3341.
36 P. Yang, Y. Zhao, Y. Lu, Q.-Z. Xu, X.-W. Xu, L. Dong and S.-H. Yu, *ACS Nano*, 2011, **5**, 2147–2154.
37 P. Yang, W. Sun, Z. Zhang and H. Xing, *Luminescence*, 2022, **37**, 1873–1880.
38 C. Q. Li, M. F. Zhang, H. B. Zuo, J. C. Han and S. H. Meng, *J. Inorg. Mater.*, 2008, **23**, 1131–1134.